Superlattices and Microstructures 126 (2019) 158–173

Contents lists available at ScienceDirect

Superlattices and Microstructures

journal homepage: www.elsevier.com/locate/superlattices

Preparation characterization and magnetic properties of $Zn_{(1-x)}Co_xO$ nanoparticle Dilute magnetic semiconductors

Kapil Y. Salkar[a], R.B. Tangsali[a,*], R.S. Gad[b], M. Jeyakanthan[a], Uma Subramanian[a]

[a] Department of Physics, Goa University, Taleigao Plateau, Goa, 403206, India
[b] Department of Electronics, Goa University, Taleigao Plateau, Goa, 403206, India

ARTICLE INFO

Keywords:
Nanoparticles
Dilute magnetic semiconductors (DMS)
Photoluminescence lifetime
Hysteresis
Ferromagnetism

ABSTRACT

Cobalt-doped ZnO nanoparticles having chemical formula $Zn_{(1-x)}Co_xO$ (x = 0.05, 0.10, 0.15, 0.20) were prepared by means of auto-combustion synthesis. Formation of monophasic wurtzite structure material was confirmed from XRD data. Inclusion of the Co^{2+} ions in the ZnO matrix produced several fascinating effects in the structural, physical and magnetic properties of the nanoparticles. The lattice constants '*a*' and '*c*' got inflated and the average crystallite size shriveled from 25 nm to 17 nm with the increase of Co concentration '*x*' in the sample. The FT-IR spectra showed the characteristic absorption bands in the range of 400 cm^{-1} to 576 cm^{-1} due to formation of Zn−O and Co−O stretching bonds in the samples. Scanning Electron Microscope (SEM) images show agglomerates of particles that are spherical in nature. Energy dispersive spectroscopy (EDS) spectra of the samples giving molecular weight percentages of the elements Zn, Co and O in the samples are in agreement with the calculated percentages within the limit of permissible error. Hysteresis, FC, and ZFC measurements made on the samples, exhibit presence of ferromagnetic phase in the materials. Energy band gap estimates made with the help of UV spectroscopy indicated a decreasing trend of band gap with increasing '*x*' in the sample. Photoluminescence studies carried out with excitation wavelength of 318 nm gave several emission peaks ranging from green to violet emissions. This observation confirms the presence of vacancies (defects) in the nanoparticle samples. Luminescence decay time recorded was in the range microseconds for all the samples.

1. Introduction

Diluted magnetic semiconductor (DMS) materials are of cosmic interest because of their unique selective properties and emerging applications. Major investigations on DMS materials are focused on metal oxides, doped metal oxides, chalcogenide semiconductors, and superparamagnetic iron oxide nanoparticles [1]. In case of doped materials, it is well established that their magnetic properties strongly depend on the type and quantity of dopant material, the preparative method adopted and the conditions at preparation [2]. DMS materials are usually obtained by introducing a small amount of transition metal ions into the semiconductor host. These types of materials are known to exhibit useful semiconductor and magnetic properties simultaneously. These materials have many useful applications in the area of biomedical sensors, magnetic resonance imaging and an ultra new emerging area of electronics known as spintronics. Spintronics is an area wherein both electron charge and spin can be explored for electronic communication [1,3], unlike conventional semiconductors where electron charge forms the main component of conduction. Zinc Oxide (ZnO) a popular material

* Corresponding author.
E-mail address: rbtangsali@unigoa.ac.in (R.B. Tangsali).

https://doi.org/10.1016/j.spmi.2018.12.013
Received 7 September 2018; Received in revised form 30 November 2018; Accepted 10 December 2018
Available online 12 December 2018
0749-6036/

found in abundance in nature and easy to prepare in the laboratory is being investigated on a large scale.

Group II-VI semiconducting materials such as cadmium selenide (CdSe), cadmium sulphide (CdS), zinc sulphide (ZnS), zinc selenide (ZnSe), and zinc oxide (ZnO) own some unique properties highly useful for several applications [4,5]. Among these materials, ZnO has a stable hexagonal wurtzite structure with n-type electrical conductivity which is most suitable as a DMS material for spintronics applications [8]. Moreover ZnO with wide band gap of 3.37 eV and high exciton binding energy of 60 meV becomes attractive for many optical applications [6,7]. Doping with transition elements like Cr, Mn, Fe, Co, Ni, or rare earth elements such as Nd, Eu, Gd enhances the semiconducting properties which makes it more effectual for the development of novel magneto-electronic and opto-electronic devices [7,9]. The incredible characteristics of ZnO makes it an important material in fields like cosmetics, gas sensors, biosensors, storage devices, optical and electrical devices, solar cells, and also drug delivery systems [10,11]. Due to the precise doping possibilities, ZnO enjoys superior potential for transparent oxide and high-temperature applications [1].

Currently transition metal and rare earth doped metal oxide materials such as ZnO, TiO_2, SnO_2, In_2O_3 as DMS materials have generated great curiosity and are being investigated to testify its possible application as future spintronics materials [2,12]. Several reports on use of dopants like Cr, Mn, Fe, Co, Eu, Gd for production of doped ZnO nanoparticles, thin films and bulk material have been published [12–14]. Recently T. J. Castro et al. and Yinyun Lü et al. have reported that ferromagnetic ordering in Co-doped ZnO nanoparticles is due to inclusion of Co in ZnO matrix [15,17]. However Anshu Singhal et al. in his report states that the activation of ferromagnetism in Co and Ni -doped ZnO nanocrystals prepared by nonhydrolytic alcoholysis esterification elimination reaction depends on defects developed in the material [16]. Anindita Samanta et al. have revealed that oxygen and Zinc related defects are the main causes for induction of ferromagnetism in the cobalt-doped ZnO samples synthesized via chemical precipitation method [18]. S.H.U. Yuldashev et al. have investigated the origin of ferromagnetism in cobalt-doped ZnO thin films, the report suggests that the occurrence of ferromagnetism is due to uncompensated magnetic moment arising from CoO nanoclusters embedded in the material [19]. A thoughtful perception of the reports shows that occurrence of ferromagnetism in Co-doped ZnO is still a conjecture. These studies do not provide a logical picture but a confused approach of the occurrence of ferromagnetism and other properties observed in Co-doped ZnO nanoparticles.

The present article is a report on in-depth investigations carried out on structural magnetic and optical properties of Co-doped ZnO nanoparticles prepared by combustion method. The auto-combustion method of sample preparation was preferred as it is simple, involves minimal equipment, low grade chemicals, takes less preparation time and yields high purity material. The samples were characterized with usual experimental techniques to establish the formation of monophasic nanoparticle sample with appropriate stoichiometry prior to investigations of various properties of the samples. Investigations on structural, magnetic and optical properties of these materials have revealed interesting and exciting conclusions. The results presented and the deductions arrived at, do provide a more logical approach as these differ from the ones that are reported. The lattice constants, bond lengths and cell volume are found to enhance with increment in Co^{2+} concentration. The material exhibits diamagnetic nature at lower doping concentration and undulates into ferromagnetic magnetization as the concentration '*x*' is raised from 0.05 to 0.20. The evidence of ferromagnetism in the samples comes from the hysteresis, ZFC and FC measurements carried out on the nanoparticle samples. The energy band gap and the luminescence decay times in microseconds that dwindle with increase in the Co^{2+} concentration '*x*' in the material nevertheless provide passable support to conclude that Co^{2+} ions have actually gone in the ZnO matrix filling the vacancies created by shortfall of Zn ions. Thus the report provides a comprehensive study on nanoparticle Co doped ZnO DMS material enriched with interesting findings.

2. Experimental procedures

2.1. Materials preparation

Ultrafine particles of $Zn_{(1-x)}Co_xO$ (x = 0.05, 0.10, 0.15, 0.20) were prepared using auto-combustion method of sample preparation [20,21]. Metal salts that include zinc acetate [$C_4H_6O_4Zn.2H_2O$], Cobalt (II) acetate tetrahydrate [$(CH_3COO)_2.Co.4H_2O$] taken in stoichiometric proportions along with Nitrilotriacetic acid (NTA) [$C_6H_9NO_6$] and Glycine [$NH_2.CH_2.COOH$] taken in appropriate proportions were dissolved in double distilled water. The solute in the solution was thoroughly mixed using a magnetic stirrer maintained at 90 °C to obtain a homogeneous solution. The homogeneous solution was further heated on the magnetic stirrer at 100 °C for reduction of water content until it turns in to a thick viscous solution. The viscous solution was transferred to a shallow plate that was placed on a heater. The solution was stirred continuously to minimize the effect of the temperature gradient within the content. Continuation of heating makes the solution glutinous turning it into a thick dry mass which self-ignites to produce a greenish colored ultrafine powder, which is the required sample. All samples were prepared following this method that enjoys several benefits of being simple, cost effective as one can use lower grade chemicals, quick as it consumes less time and yield efficient as the sample yield is high [69].

2.2. Characterization

X-ray powder diffraction technique forms an integral part of samples characterization process. One can determine the material structure, purity of phase and crystallite size of the material in addition to other important information like cation distribution and X-ray density. Room temperature X-ray diffraction (XRD) patterns for all the samples were recorded on Rigaku X-ray diffractometer with Molybdenum target using K_α radiation with wavelength λ = 0.7093 Å. Since the wavelength is low, scanning range was set between 10° to 40° with 2θ varying in steps of 0.02° at a scan rate of 2°/min. Rietveld refinement of XRD data was done using FullProf

suite software. Fourier transform infra red (FTIR) absorption spectra of the samples in the wave number range of 400 cm^{-1} to 2500 cm^{-1} was obtained on SHIMADZU IR-800 Spectrometer by utilizing standard technique. The scanning electron microscope CARL ZEISS EVO 18 was utilized to obtain SEM images and EDS spectra of the nanopowders whereas transmission electron microscope (TEM) images were obtained on TECHNAI G2 TEM with an accelerating voltage of 200 kV. The magnetic property measurements were carried out at room temperature on Quantum Design's Versa Lab 3T vibrating sample magnetometer (VSM). A small quantity of sample weighing 5 mg was wrapped in Teflon tape and mounted on the sample holder for obtaining the hysteresis measurements. The corrected data was obtained after eliminating the contribution of Teflon tape that was determined initially prior to loading of the sample. Zero field cooled (ZFC) and field cooled (FC) magnetic moment data on the samples was obtained on the same VSM setup. For obtaining Zero field cooled (ZFC) magnetic moment data, the sample was first cooled down from room temperature to 50 K in absence of magnetic field, subsequently precise magnetic moment of the sample was recorded by increasing the temperature of the sample in presence of constant applied magnetic field of 500 Oe. For obtaining field cooled (FC) magnetic moment data, the sample was cooled from room temperature to 50 K with a magnetic field of 500 Oe and the required data was recorded as the sample warms up. The complete measurement is automated and computer controlled through a software program which is adjusted by feeding in the required parameters. Energy band gap of the samples was obtained from UV–visible absorption spectroscopy done in reflectance mode on Shimadzu 2401 PC UV Spectrophotometer. Adequate quantity of sample powder was pressed into the sample holder and mounted on the spectrometer which is radiated with UV radiation in the wavelength range of 300 nm–800 nm. The photoluminescence spectra and lifetimes were recorded using PTI Spectrofluorometer QM-40. A 150 W steady xenon lamp source was used to obtain the photoluminescence data whereas 150 W pulsed xenon source was used for recording the photoluminescence lifetime data. The excitation wavelength of 318 nm was utilized for recording of photoluminescence spectra and the decay times or the lifetimes of all emission wavelengths observed in the emission spectra.

3. Result and discussion

3.1. X-ray diffraction

Typical X-ray diffraction patterns acquired on the samples $Zn_{(1-x)}Co_xO$ (x = 0.05, 0.10, 0.15, 0.20) are shown in Fig. 1. Since the X-ray beam is generated by Molybdenum target with wavelength λ = 0.7093 Å and not from Copper target having wavelength λ = 1.5418 Å, the inter planer spacing 'd' values evaluated from the data and the 'd' values obtained from the standard data (JCPDS-79-2205) for Cu target with λ = 1.5418 Å are tabulated in Table 1. The lattice constant values 'a' and 'c', bond lengths 'l' and cell volume 'V' obtained, shown in Fig. 2, Fig. 3 and Fig. 4 respectively are found to be in excellent agreement with the reported data [22–24]. Consistency in the conformity of inter planer distance 'd', the lattice constants values and the bond length values with reported data authenticates formation of monophasic wurtzite phase samples. This also ascertains successful substitution of Co^{2+} ions in place of Zn^{2+} ions sites inside ZnO matrix [22,23,25]. Dominance of ⟨101 > peak in all XRD patterns, with intensity higher than that of the other peaks suggests superior growth of ⟨101 > orientation along c-axis [26,27].

The variation of 'a', 'c' with Co concentration 'x' presented in Fig. 2 shows responsiveness of these parameters to inclusion of Co^{2+} ions in ZnO matrix. There is a minor rise in both the lattice constants 'a' and 'c' when 'x' increases from 0.05 to 0.10 and 0.15 to 0.20. However, there is a drastic enlargement in their values when 'x' changes from 0.10 to 0.15 which is unique and interesting, such trends are far from reported results. This type of unique variation is also observed in bond length shown in Fig. 3 and cell volume in Fig. 4. As per Hermann–Mauguin notation the wurtzite structure ZnO has a hexagonal unit cell with lattice parameters 'a' and 'c' in the ratio of $c/a = (8/3)^{1/2} = 1.633$ in an ideal case, belong to $P6_3mc$ space group. In the current investigations, the ratio c/a equals 1.632 for all the samples and matches with the ideal value. Increasing trends of both the parameters 'a' and 'c' reveals that Co^{2+} has entered into the octahedral environment in the wurtzite structure and it has drastically enhance the parameters leading to a disorder

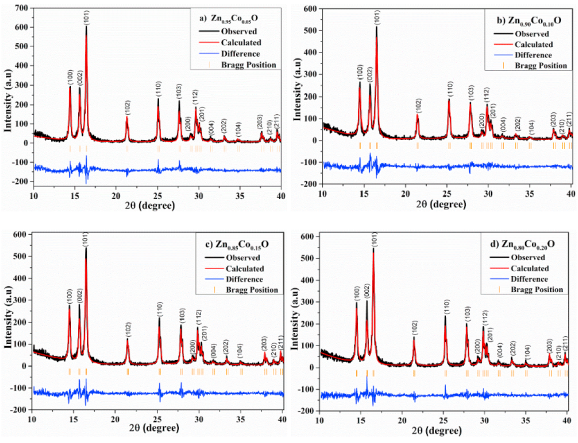

Fig. 1. Rietveld refined XRD patterns of $Zn_{(1-x)}Co_xO$ with (a) x = 0.05, (b) x = 0.10, (c) x = 0.15, (d) x = 0.20.

Table 1
Comparison of '*d*' spacing from JCPDS-79-2205 with Rietveld refinement data obtained on nanoparticle $Zn_{(1-x)}Co_xO$ (x = 0.05, 0.10, 0.15, 0.20).

hkl	*d* spacing in Å	*d* spacing in Å (Rietveld refinement)			
	(JCPDS-79-2205)	$Zn_{0.95}Co_{0.05}O$	$Zn_{0.90}Co_{0.10}O$	$Zn_{0.85}Co_{0.15}O$	$Zn_{0.80}Co_{0.20}O$
100	2.814	2.835	2.838	2.851	2.854
002	2.606	2.627	2.627	2.631	2.634
101	2.478	2.497	2.499	2.502	2.504
102	1.912	1.923	1.923	1.928	1.928
110	1.626	1.633	1.634	1.638	1639
103	1.478	1.484	1.484	1.486	1.489
200	1.408	1.413	1.416	1.417	1.421
112	1.379	1.384	1.385	1.388	1.388
201	1.359	1.243	1.308	1.247	1.310
004	1.302	1.096	1.100	1.099	1.101
202	1.239	1.046	1.049	1.049	1.049

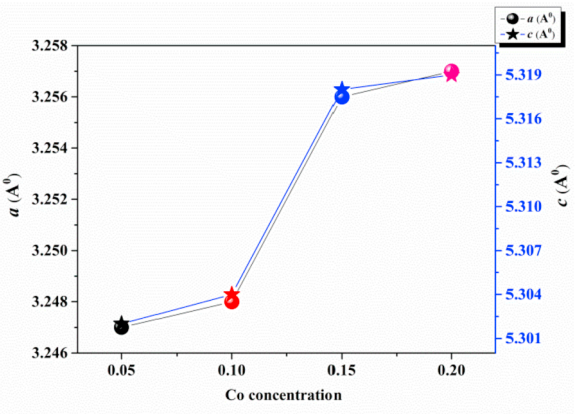

Fig. 2. Variation of lattice constant '*a*' and '*c*' with Co concentration.

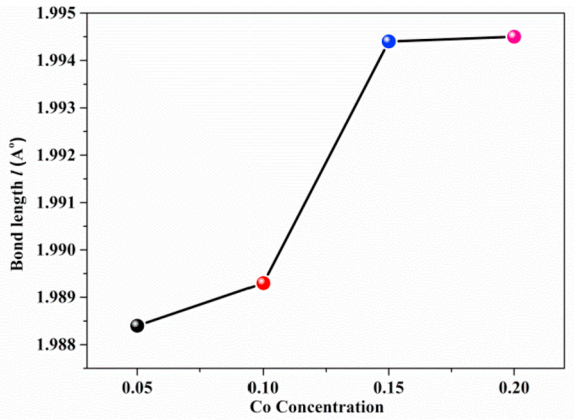

Fig. 3. Variation of Bond length '*l*' with Co concentration.

in the lattice. It may be noted that when Co^{2+} is in the octahedral environment in the low spin state, it has ionic radius of 0.65 Å but when in high spin state it has an ionic radius of 0.745 Å both of which are larger than Zn^{2+} ionic radius of 0.60 Å [25,28].

The internal parameter '*u*', nearest neighbor Zn—O bond length '*l*', in wurtzite structure and the unit cell volume 'V' for the hexagonal structure are obtained using equations (1)-(3) respectively.

$$u = \frac{1}{3}\left(\frac{a^2}{c^2}\right) + \frac{1}{4} \tag{1}$$

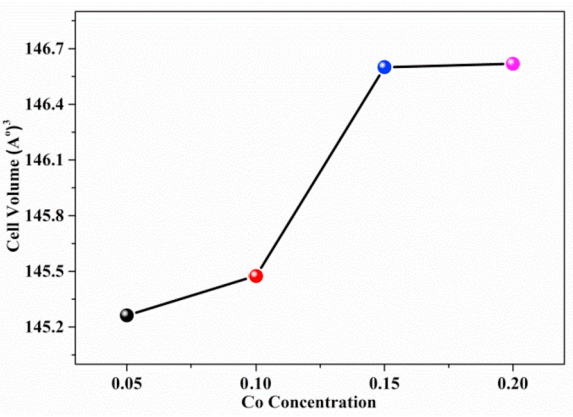

Fig. 4. Variation of Unit Cell Volume 'V' with Co concentration.

$$l = \sqrt{\frac{a^2}{3} + (\frac{1}{2} - u)^2 c^2} \tag{2}$$

$$V = \frac{3\sqrt{3}}{2} a^2 c \tag{3}$$

The variation of bond length '*l*' and the unit cell volume 'V' with '*x*' is depicted in Figs. 3 and 4. It may be observed that '*l*' increases from 1.988 Å to 1.994 Å whereas 'V' increases from 145.263 $Å^3$ to 146.617 $Å^3$ as '*x*' enhances from 0.05 to 0.20. The flare-up in these values with enhancement in '*x*' is essentially due to Co^{2+} mending in high spin state in octahedral environment of the wurtzite structure during the material formation process [29,30]. A close examination of bond length '*l*', cell volume 'V', and the lattice constants '*a*', '*c*' demonstrate identical rising trends as '*x*' increases from 0.05 to 0.20 in the nanoparticle samples. These facts provide the required conclusive substantiation that all of Co^{2+} added goes in to high spin state in the material.

The crystallite size was determined using Williamson-Hall analysis and size-strain plot method using equation (4).

$$\beta cos\theta = \frac{k\lambda}{t} + 4\varepsilon sin\theta \tag{4}$$

Where, β is the full width at half the maximum intensity of the XRD peaks in radians, θ is half of the angle 2θ at peak position in degrees, k is the shape factor (0.9), λ is the wavelength of X-rays, '*t*' is the crystallite size in nm and ε is the strain. The values of $\beta cos\theta$ were plotted against $4sin\theta$ and the intercept was used to obtain the crystallite size (t) [31,32]. The crystallite size '*t*' shown in Fig. 5 as a function of '*x*' is seen to decrease with '*x*' which may be due to the fact that, the growth of nanoparticles during the formation of the samples is impaired by slowing down the movement of the grain boundaries following increased pinning effect of fine pores in the samples [33,34]. When the moving boundaries connect the pores, the particle growth is hindered by generating a retarded force, a phenomenon termed as Zener-pinning effect. The retarding force generated at the boundary is proportional to the boundary length attached to these ions and the pores. The maximum force generated by a single pore on such a moving boundary is $F_{max} = \Pi r_p \gamma_b$ where γ_b is the grain boundary energy and r_p is the obstacle radius [34]. Thus the particle growth is stalled when the retarded force overwhelms the driving force enforcing grain growth. Therefore the inclusion of Co^{2+} ions in the ZnO matrix creates impediments for grain growth which increases with Co concentration thereby lowering grain size as visible in Fig. 5. Thus the enhancement of doping concentration indirectly helps in keeping a lower particle size.

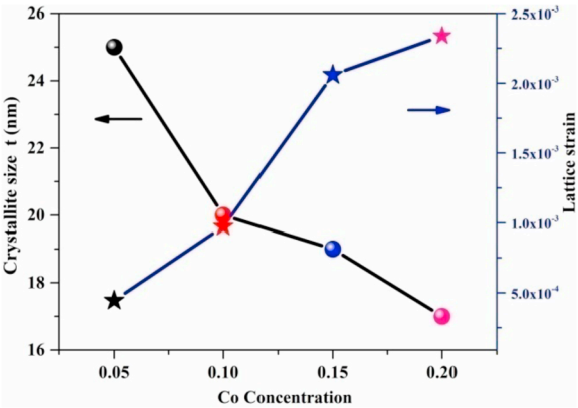

Fig. 5. Variation of Crystallite size '*t*' and Lattice strain with Co concentration.

3.2. Particle size estimation from SEM and TEM micrographs

Scanning electron microscopy (SEM) and Transmission electron microscopy (TEM) are essential tools that provide information about microstructure and help in estimating the average particle size of the material. Room temperature SEM micrographs of the sample $Zn_{(1-x)}Co_xO$ (x = 0.05, 0.10, 0.15, 0.20) are shown in Fig. 6. The micrographs show agglomerates of the nanoparticles that are spherical in shape with typical particle size ranging from 25 nm to 55 nm. However an average particle size of 21 ± 3 nm was obtained from the TEM micrograph of the sample $Zn_{0.85}Co_{0.15}O$ shown in Fig. 6. (e). The estimate arrived at by using Image J software, over an ensemble size of 50 particles is in good agreement with crystallite size obtained from XRD data. This analysis of SEM and TEM micrographs confirms formation of nanoparticle material.

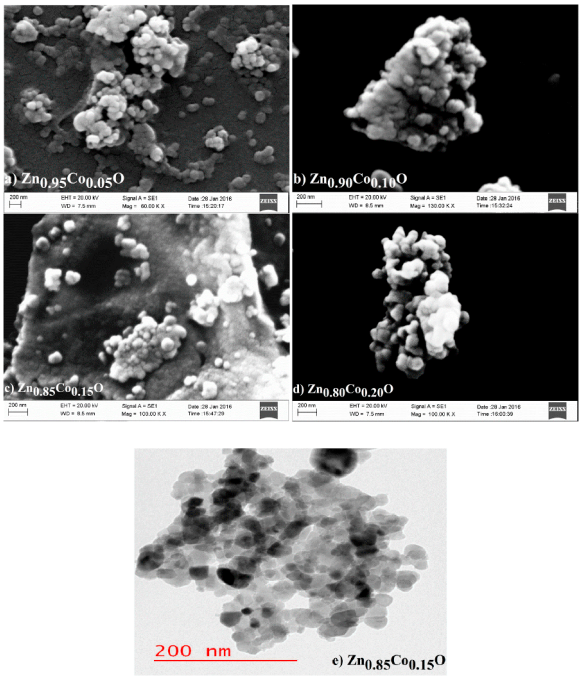

Fig. 6. SEM micrographs of (a) $Zn_{0.95}Co_{0.05}O$, (b) $Zn_{0.90}Co_{0.10}O$, (c) $Zn_{0.85}Co_{0.15}O$, (d) $Zn_{0.80}Co_{0.20}O$ and e) TEM image of $Zn_{0.85}Co_{0.15}O$ at room temperature.

The elemental composition of (a) $Zn_{0.95}Co_{0.05}O$, (b) $Zn_{0.90}Co_{0.10}O$, (c) $Zn_{0.85}Co_{0.15}O$, (d) $Zn_{0.80}Co_{0.20}O$ has been analyzed using the energy dispersive spectroscopy (EDS). The EDS spectra obtained on all the samples are shown in Fig. 7. The EDS pattern attests the existence of Zn, Co and O elements with no other impurity element in the nanosamples. Experimental and calculated elemental

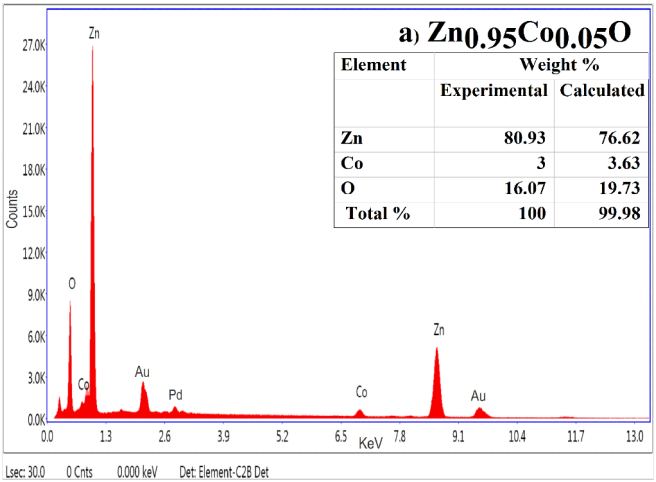

Fig. 7. EDS analysis of (a) $Zn_{0.95}Co_{0.05}O$, (b) $Zn_{0.90}Co_{0.10}O$, (c) $Zn_{0.85}Co_{0.15}O$, (d) $Zn_{0.80}Co_{0.20}O$.

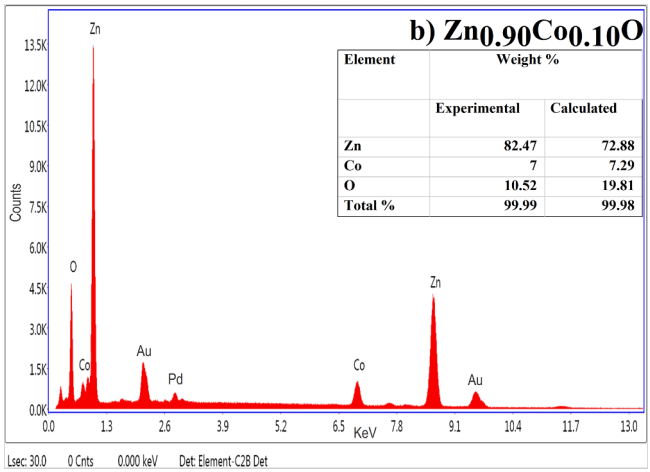

Fig. 7. (*continued*)

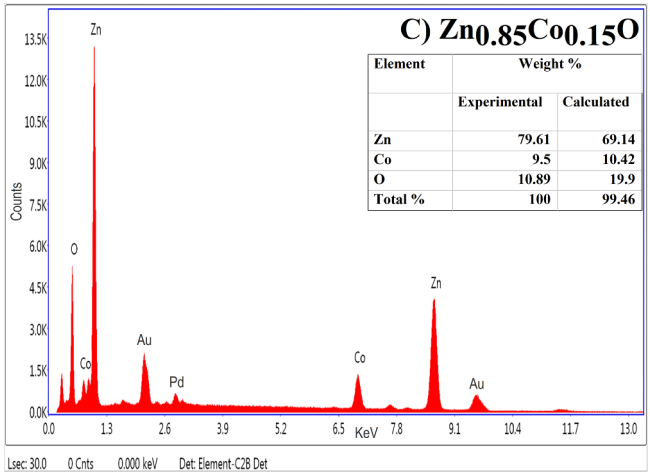

Fig. 7. (*continued*)

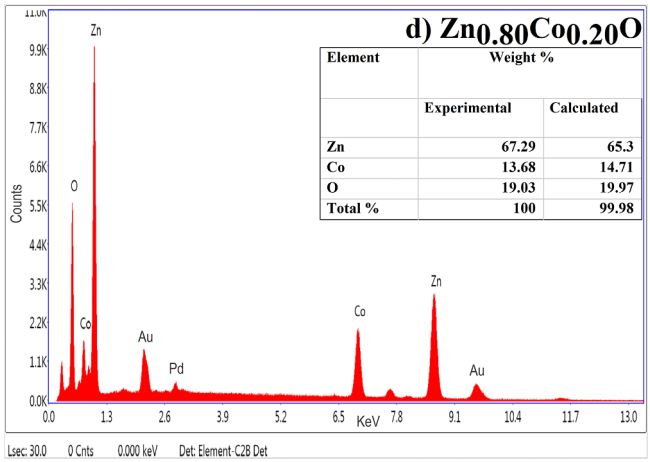

Fig. 7. (*continued*)

weight percentages in all the samples displayed in the inserts Fig. 7 are in good agreement within the limits of experimental errors. EDS pattern further provides the obligatory evidence of successful substitution of Co^{2+} ions into the ZnO matrix ruling out the possibility of additional trace impurities entering the material.

3.3. Fourier Transform Infra-red spectroscopy

Fourier Transform Infra-red spectroscopy (FTIR) is an essential tool in materials characterization that is capable of identifying the presence of impurity traces in the freshly prepared materials. Different elemental bonds that exist in compounds vibrate/rotate at different frequencies that fall in infra-red region. Exposure of these materials to IR energy gives rise to resonance absorption bands in the FTIR spectra. FTIR spectra of $Zn_{(1-x)}Co_xO$ (x = 0.05, 0.10, 0.15, 0.20) were recorded at room temperature using KBr pellet method. Several stretching and vibrational bonds can be identified from the FTIR spectra presented in Fig. 8. One can identify two main absorption bands first one in the range of 400 cm^{-1} to 576 cm^{-1} and the second in the range of 650 cm^{-1} - 700 cm^{-1}. These bands are attributed to the Zn−O stretching bonds and Co−O vibrational bonds in the lattice. The occurrence of second band is due to addition of Co^{2+} into the Zn−O lattice [35,36]. In addition to the two main absorption bands another set of three small absorption bands in the range of 1385 cm^{-1} to 1400 cm^{-1}, 1550 cm^{-1} – 1680 cm^{-1}, and 2280 cm^{-1} to 2390 cm^{-1}, could be also identified and are listed in Table 2. The absorption band in between 1385 cm^{-1} to 1400 cm^{-1} corresponds to the asymmetrical and symmetrical stretching vibration of the carboxylate group (COO^-) that could be originating from fuel Glycine [$NH_2.CH_2.COOH$] [24,37]. The sample for FTIR spectra is prepared by mixing it with hygroscopic KBr which results in an absorption band between 1550 cm^{-1} – 1680 cm^{-1} due to H−*O*−H bending vibration [38]. Absorption band in the range 2280 cm^{-1} to 2390 cm^{-1} corresponds to the bending of CO_2 molecule that is present in the air [38,39].

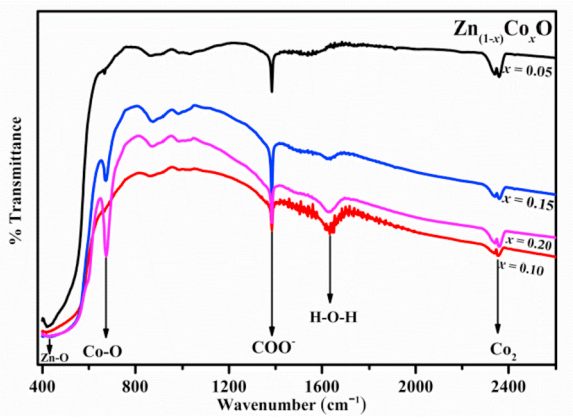

Fig. 8. Fourier transforms infra red spectra for $Zn_{(1-x)}Co_xO$ (x = 0.05,0.10,0.15,0.20) at room temperature.

Thus identification of bonds like Zn-O and Co-O along with their characteristic vibrational frequencies from FTIR spectra confirms formation of impurity free monophasic sample.

3.4. Magnetic Properties

The results of room temperature magnetic hysteresis measurements made on the samples are shown in Fig. 9. The inserts in the figure show the enlarged view of the hysteresis curves near origin. The sample with lowest Co^{2+} concentration retains the diamagnetic behavior of ZnO whereas the other three samples with higher Co^{2+} concentration exhibit ferromagnetic behavior. This implies that introduction of trace amount of Co (x = 0.05) is incapable of altering the diamagnetic behavior of the sample [40]. The largest magnetic moment is observed for sample containing highest Co^{2+} concentration [41,42]. The magnetization of these samples advances linearly above 2–3 kOe of the applied field. The linear increase of magnetization in the M-H loops can be explained on the basis of strong d-d exchange interaction coupled with Co^{2+} ions which increases with increase in Co^{2+} doping. At low level (x = 0.05) of Co^{2+} doping, d-d exchange interaction if present is very weak and limits the sample from going into a ferromagnetic state. Thus the Co^{2+} doped samples at this concentration level do not exhibit ferromagnetism. The origin of increasing magnetization

Table 2
FTIR vibration band frequencies of $Zn_{(1-x)}Co_xO$ (x = 0.05, 0.10, 0.15, 0.20) nanoparticles.

Sample	Zn−O Stretching Mode (Cm^{-1})	Zn−*O*−Co Stretching Mode (Cm^{-1})	carboxylate group Stretching (Cm^{-1})	H−*O*−H Bending Mode (Cm^{-1})	CO_2 Bending Mode (Cm^{-1})
$Zn_{0.95}Co_{0.05}O$	418	667	1384	1556	2359
$Zn_{0.90}Co_{0.10}O$	416	667	1384	1633	2359
$Zn_{0.85}Co_{0.15}O$	441	675	1384	1629	2359
$Zn_{0.80}Co_{0.20}O$	447	675	1384	1626	2359

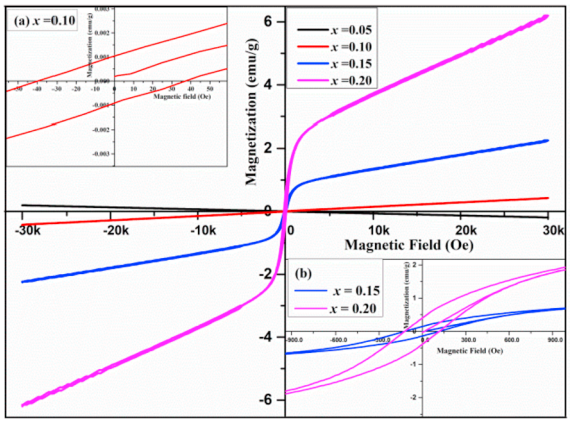

Fig. 9. Hysteresis loop of $Zn_{(1-x)}Co_xO$ (x = 0.05, 0.10, 0.15, 0.20) at room temperature.

in the M-H loops at higher concentrations of x = 0.15, 0.20 can be explained on the basis of Co^{2+} going in the high spin state. Co^{2+} ($4s^03d^7$) ions in high spin state configuration has three unpaired electrons as shown in Fig. 10, this creates a high spin environment in the wurtzite structure leading to enhancement in the magnetization [52]. Thus for samples with x = 0.15 and 0.20 the high spin environment and strong d-d exchange interaction rapidly enhances the magnetization giving rise to ferromagnetism in these samples. Although the samples with x = 0.10, 0.15, 0.20 exhibit ferromagnetism which is higher in magnitude, the samples are far from attaining a stable saturation state [43,44].

To investigate the perspective aspect about the magnetic behavior in nano DMS materials, variation of magnetization with respect to temperature (M-T curves) were obtained under zero field cooled (ZFC) and field cooled (FC) conditions with an applied magnetic field of 500 Oe. The magnetization of the samples as seen from Fig. 11 is found to decrease with increasing temperature. This is due to

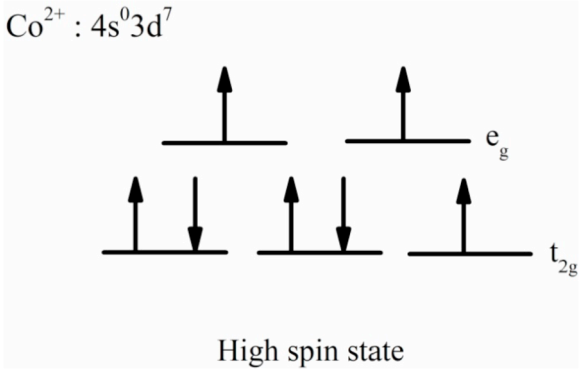

Fig. 10. Co^{2+} ($4s^03d^7$) high spin electronic configuration.

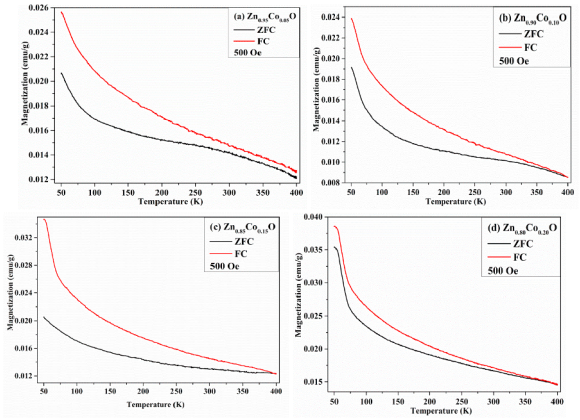

Fig. 11. Zero field cooled (ZFC) and Field cooled (FC) Plots for $Zn_{(1-x)}Co_xO$ with (a) x = 0.05, (b) x = 0.10, (c) x = 0.15, (d) x = 0.20 under 500 Oe.

increase in thermal agitation of the atoms which results in non-alignment of the atoms in the magnetic field. Normally a decrease in magnetization with increasing temperature is an indication of the paramagnetic behavior of a material [45]. However at a given temperature, the difference between the corresponding magnetization value on FC and ZFC curves gives the net ferromagnetic contribution of the sample by deducting paramagnetic and diamagnetic contributions at that temperature [46]. In the present case, the distinct separation between FC and ZFC curves with the presence of irreversibility temperature of 398 K, 395 K and 389 K for last three samples indicates presence of ferromagnetic ordering in these samples. It may be seen that decrease of irreversibility temperature with increase in Co^{2+} concentrations is an indicator of an increase in ferromagnetic ordering. This behavior can very clearly be seen in the hysteresis curves given in Fig. 9.

For a sample with $x = 0.05$ irreversible temperature could not be seen till 400 K which is the limit of the instrument. This may be due to the low value of doping concentration which can be also visible from the M-H curve in Fig. 9. Moreover, the smooth fall of ZFC and FC curves with rising temperature without any cusp indicates absence of characteristic FM to SPM or FM to PM transition [47,48]. Since the samples are free from impurity phases such as CoO or Co_3O_4, no antiferromagnetic ordering was observed that is normally rampant in presence of these types of impurities that annihilates ferromagnetism in materials [49]. Thus the natures of FC and ZFC curves supports formation of impurity free material and justify induction of ferromagnetism in the samples which is exclusively due to exchange interactions between the localized d-electrons in Co^{2+} atoms.

3.5. UV–visible spectroscopy

UV absorption spectra of the samples $Zn_{(1-x)}Co_xO$ ($x = 0.05, 0.10, 0.15, 0.20$) measured at room temperature in the wavelength range 300 nm - 800 nm is shown in Fig. 12(a). These measurements were performed to study the effect of Co^{2+} doping on the band gap of the material and to testify the substitution of Co^{2+} in the ZnO structure. It is observed that absorbance is maximum for lower Co^{2+} concentration and decreases slowly with increasing Co^{2+} concentration in ZnO. It is known that total UV absorbance depends on factors like lattice strain, crystallite size, oxygen deficiency, impurity centers, surface roughness, agglomeration of the nanoparticles etc [70]. Particle size dependent agglomeration of particles in the samples restricts the sample area exposed to the radiation. It can be seen from Fig. 5 that increase of lattice strain with Co^{2+} concentration 'x' restricts the crystallite growth thereby reducing the crystallite size in the sample. Thus reduction in crystallite size will result in reduced UV absorption that is being reflected in the energy band gap of the systems. Secondly PL studies show reduction in peak intensities with increasing 'x' which implies that oxygen deficiency in the samples decreases as Co^{2+} content increases in the samples. Moreover X-ray and EDS affirm formation of impurity free samples. Consequently these observations provide adequate evidence on reduction of UV absorbance with increasing Co^{2+} concentrations in the samples [70,71].

Three additional humps at 568 nm (2.18eV), 612 nm (2.03eV) and 660 nm (1.88eV) are observed for all samples as shown in Fig. 12(a). These humps are due to d-d_6 electronic transitions which are known to occur from the ground state $^4A_2$ to $^2A_1$, $^4T_1$ and $^2E_1$

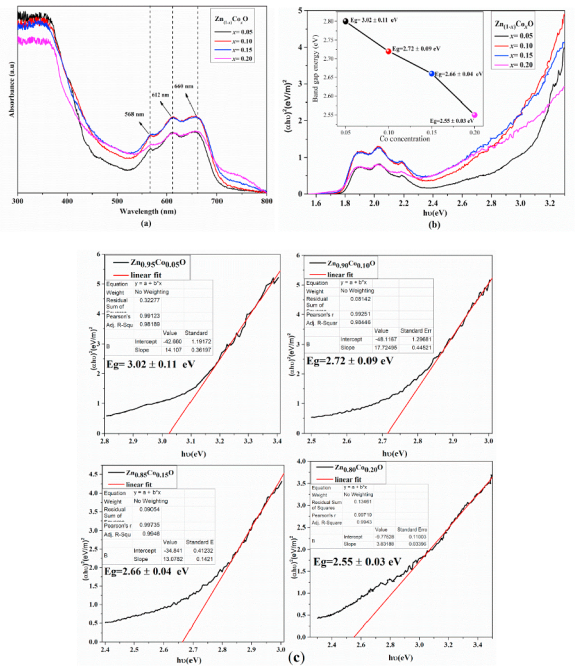

Fig. 12. (a) UV absorbance spectra, (b) Plots of $(\alpha h\nu)^2$ versus photon energy ($h\nu$), (c) linear regression fit for $Zn_{(1-x)}Co_xO$ ($x = 0.05, 0.10, 0.15, 0.20$).

state for the tetrahedral Co^{2+} ions [50,51]. The presence of Co^{2+} in high spin state at tetrahedral environment is known to create lattice distortion which is furthermore confirmed by X-ray studies [52]. The presence of these three peaks in the visible region indicates the successful incorporation of Co^{2+} ions in the Zn^{2+} tetrahedral sites of the ZnO matrix [50–52]. A random UV absorption effect is seen in case of absorption by d-d transition levels in the samples. Samples with $x = 0.05, 0.20$ show lower absorption then samples with $x = 0.10, 0.15$. This variation in absorbance may be due to factors like particle size, reduction in impurity centers, surface roughness and agglomeration of particles which cannot be controlled by any nanoparticles materials preparation method.

The energy band gap for Co-doped ZnO samples was calculated from Tauc's plots as per equation (5) in which A is constant, $h\upsilon$ the photon energy, E_g is the energy band gap, n = ½ for allowed direct transitions and n = 2 for allowed indirect transitions [53].

$$(\alpha h\upsilon) = A\,(h\upsilon - Eg)^n \tag{5}$$

Fig. 12(b) shows Tauc's plots $(\alpha h\upsilon)^2$ V $h\upsilon$ for the samples with the inset showing corresponding direct band gap energy values obtained. These precise band gap values of Co-doped ZnO were obtained using linear regression fit at higher energy values taken from tauc's plots as shown in Fig. 12(c). The highest energy band gap value $E_g = 3.02 \pm 0.11$ eV at $x = 0.05$ was found to decrease linearly to a value of $E_g = 2.55 \pm 0.03$ eV at $x = 0.20$ thus escalating the optical wavelength which is an indication of a red shift in the band gap [54,55]. The reduction in energy band gap with Co^{2+} concentration [insert in Fig. 12 (b)] is attributed to the exchange interaction between the localized d-electrons of Co^{2+} atoms and the s-p band electrons of ZnO [56,57].

3.6. Photoluminescence

The photoluminescence (PL) emission spectra of the sample $Zn_{(1-x)}Co_xO$ ($x = 0.05, 0.10, 0.15, 0.20$) obtained at room temperature with an excitation wavelength of 318 nm is shown in Fig. 13. In general, the overall PL intensities follow a decreasing pattern as the Co^{2+} concentration increases in the sample. The sample $Zn_{0.95}Co_{0.05}O$ shows most intense PL spectra with a wide spread in the

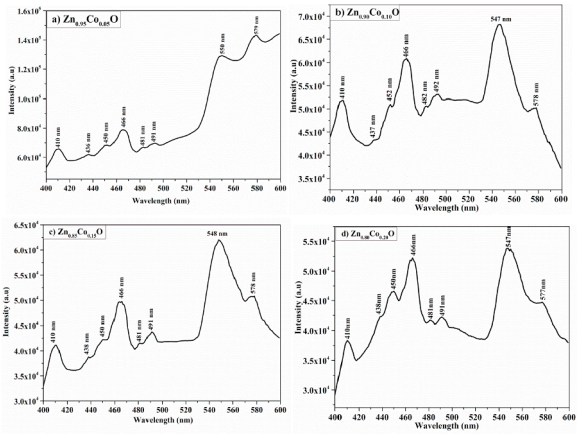

Fig. 13. Room temperature PL spectra of (a) $Zn_{0.95}Co_{0.05}O$ (b) $Zn_{0.90}Co_{0.10}O$ (c) $Zn_{0.85}Co_{0.15}O$ (d) $Zn_{0.80}Co_{0.20}O$.

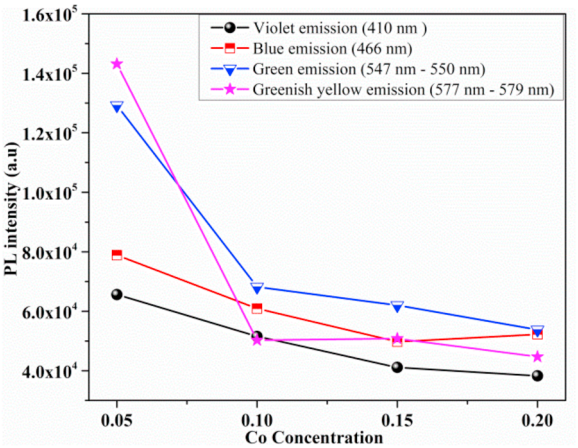

Fig. 14. Variation of PL intensity with Co concentration.

Table 3
PL emission wavelengths and intensities of $Zn_{(1-x)}Co_xO$ (x = 0.05, 0.10, 0.15,0.20) at room temperature obtained with excitation wavelength of 318 nm.

Co Concentration x	Violet Emission wavelength (nm)	Intensity (a.u)	Blue Emission wavelength (nm)	Intensity (a.u)	Green Emission Wavelength (nm)	Intensity (a.u)
$Zn_{0.95}Co_{0.05}O$	410	65602	436	61919	550	129213
			450	68197	579	143152
			466	78858		
			481	66280		
			491	69312		
$Zn_{0.90}Co_{0.10}O$	410	51868	437	43208	547	68206
			452	50977	578	50277
			466	60902		
			482	50572		
			492	53115		
$Zn_{0.85}Co_{0.15}O$	410	41120	438	38781	548	62003
			450	42214	578	50803
			466	49746		
			481	41536		
			491	43753		
$Zn_{0.80}Co_{0.20}O$	410	38309	438	42242	547	53804
			450	46588	577	44718
			466	52254		
			481	41708		
			491	42206		

greenish-yellow region. The emission spectra for higher values of Co^{2+} concentration gets more refined and is found to show specific peaks in different color regions in place of a broad spread seen between 500 nm and 600 nm. The emission wavelengths and their peak intensities are seen to become sharper and distinct with a minor slide down in overall intensities. The variation of the most intense peak intensities for wavelengths namely 410 nm, 466 nm, 547–550 nm and 579 nm as a function of Co^{2+} concentration 'x' are shown in Fig. 14. The decrease in PL intensity observed is due to the creation of defect states below the conduction band that decreases with increasing 'x' in the ZnO matrix. Some of the electrons excited from valence band slow down at the defect states without reaching the conduction band [58] resulting in decreased PL intensity. It may be seen that for a given concentration, green emission is the most intense emission except for sample with x = 0.05 where greenish-yellow emission takes the maximum intensity.

The PL emission peaks in three different regions namely violet, blue and green as shown in Table 3 have been observed for all the samples. Zinc oxide by itself has a large band gap (3.3 eV) which goes on decreasing from 3.02 ± 0.11 eV to 2.55 ± 0.03 eV due to the addition of Co^{2+} in the ZnO matrix. Reports suggest that these emissions in the visible region are result of intrinsic defects created in the samples, which include Zn vacancies (V_{Zn}), O vacancies (V_O), interstitial Zn (Zn_i), interstitial O (O_i), and intermediate levels formed between valence band and conduction band due to Co^{2+} substitution at Zn^{2+} positions [52,59].

The emission peak observed in violet region at 410 nm for all the samples is due to existence of defects such as interstitial Zn (Zn_i) and Zn vacancies (V_{Zn}) related to interface traps existing at the grain boundaries of the nanoparticles [60,61]. Five emission peaks observed in blue region (436 nm–492 nm) for all the samples, could be due to transition from interstitial Zn (Zn_i) to the valence band or transition from the bottom of the conduction band to the interstitial O (O_i) level [59,62]. Two emission peaks observed in green region (547 nm–579 nm) for all the samples, may be attributed to the presence of different types of defects such as oxygen vacancies (V_O) and zinc vacancies (V_{Zn}) in the samples [63,64].

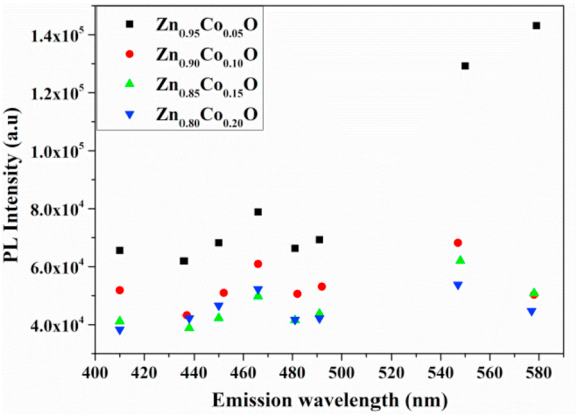

Fig. 15. Variation of PL intensity with emission wavelength for Co concentration x = 0.05, 0.10, 0.15 and 0.20.

From Fig. 15. It may be seen that PL peak positions (emission wavelengths) do not differ with variation of Co^{2+} concentration in the samples. However for any given wavelength the peak intensity decreases with increasing Co^{2+} concentration. This observation implies that the numbers of defect states or intermediate energy states are lowered on increasing Co^{2+} concentration in the sample. Secondly increase in emission intensity at higher wavelengths suggests that the defect centers or the unoccupied energy states at higher energy level close to conduction band are fewer in number compared to similar states at low energy level close to valence band. Thus it may be seen that there is no increase in the number of defect states with increase in Co^{2+} concentration in the sample.

3.6.1. Photoluminescence lifetime

Photoluminescence (PL) lifetime spectra for the sample $Zn_{(1-x)}Co_xO$, (x = 0.05, 0.10, 0.15, 0.20) was recorded at room temperature. The samples were excited with excitation wavelength of 318 nm and decay times for four prominent emission wavelengths between 410 nm and 579 nm were recorded. The PL decay curves given in Fig. 16 were fitted with single exponential function as specified by equation (6).

$$I = A \exp(-t/\tau) + I_0 \quad (6)$$

Where I_0 and I are the initial and instantaneous luminescence intensities, A is a constant, t the measurement time and τ represents the lifetime of the PL emission [65].

The calculated values of PL lifetime τ tabulated in Table 4 are in microseconds. The variation of τ and I_o with emission wavelength for the samples is shown in Fig. 17 (a) and (b) respectively. It is observed that τ for the samples show a mixed trend. The PL lifetimes on an average are seen to increase with increase in emission wavelengths for every individual sample but the order is not maintained with concentration 'x' in the samples. The short lifetime decay could be due to the radiative recombination of near-surface excitons

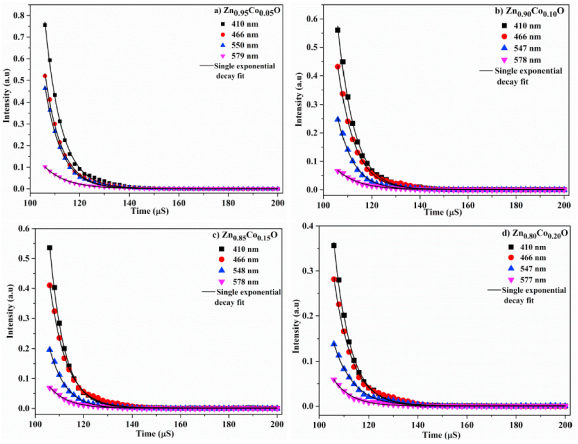

Fig. 16. PL lifetime of $Zn_{(1-x)}Co_xO$ with (a) x = 0.05, (b) x = 0.10, (c) x = 0.15, (d) x = 0.20 at room temperature with excitation wavelength 318 nm.

Table 4
Room temperature PL lifetimes observed for $Zn_{(1-x)}Co_xO$ (x = 0.05, 0.10, 0.15,0.20) with excitation wavelength of 318 nm.

Emission wavelength (nm) λ	I_o (a.u)	Lifetime τ (μS)	Emission wavelength (nm) λ	I_o (a.u)	Lifetime τ (μS)
$Zn_{0.95}Co_{0.05}O$			**$Zn_{0.90}Co_{0.10}O$**		
410	0.756	6.738 ± 0.041	410	0.560	6.637 ± 0.052
466	0.520	6.742 ± 0.040	466	0.432	6.762 ± 0.041
550	0.463	6.758 ± 0.038	547	0.247	6.962 ± 0.045
579	0.102	9.086 ± 0.048	578	0.066	8.951 ± 0.086
$Zn_{0.85}Co_{0.15}O$			**$Zn_{0.80}Co_{0.20}O$**		
410	0.536	6.138 ± 0.034	410	0.356	6.611 ± 0.039
466	0.410	7.126 ± 0.056	466	0.281	6.712 ± 0.044
548	0.196	7.403 ± 0.097	547	0.138	7.280 ± 0.068
578	0.069	7.969 ± 0.081	577	0.059	7.814 ± 0.097

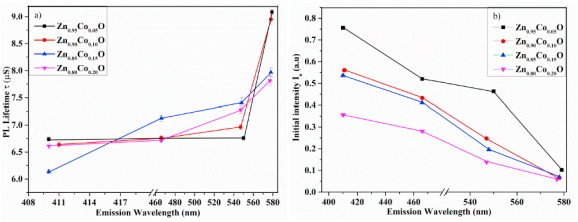

Fig. 17. (a) Variation of PL lifetime τ (μS) and (b) Variation of PL Initial intensity I_o with emission wavelength for $Zn_{(1-x)}Co_xO$ with $x = 0.05, 0.10, 0.15, 0.20$.

and due to the presence of surface defects [66,67]. The long lifetime decay for emission wavelengths in the range 466 nm–579 nm, could be due to donor-acceptor pair recombination [68]. Fig. 16 (b) shows that the initial Intensity I_o decreases with increase in Co^{2+} content and rise in emission wavelength.

4. Conclusion

Investigations were carried out on nanoparticle Co^{2+} doped ZnO DMS material prepared using auto combustion method. Formation of single-phase hexagonal wurtzite structured nanoparticle material was confirmed by using XRD, FTIR, SEM, EDS and TEM spectroscopy. Rietveld refinement using FullProf software was performed on XRD data obtained on the samples. Enhancement of structural parameters like lattice constants, bond lengths and cell volume with increase in Co^{2+} concentration has been attributed to substitution of Zn^{2+} with Co^{2+} that goes in to high spin state with bigger ionic radius in the matrix. The constant value of c/a ratio that is in proximity to the ideal value of $c/a = 1.633$ for all the samples indicates that Co-doped ZnO matrix is formed with minimum distortion in the crystal structure. Reduction in crystallite size was observed due Zener-pinning effect in the material that hinders the crystallite growth and nucleation process. SEM Micrograph shows agglomerates or clusters of the nanoparticles that are almost spherical in shape. EDS spectra further substantiates formation of materials with Zn, Co and O as the only constituent elements with appropriate proportions in the nanosamples. Formation of nanoparticle samples was confirmed from TEM micrographs. Magnetic studies carried out showed that at lowest Co concentration the sample exhibits diamagnetic phase which changes to ferromagnetic phase as the concentration '*x*' is raised from 0.05 to 0.20. Thus doping of ZnO with Co^{2+} magnetic ions introduces a spin property in the host material which is evident from FC and ZFC curves. UV–visible spectra show that replacement of Zn^{2+} ions by Co^{2+} ions produces materials with reduced energy bang gap that changes from 3.02 ± 0.11 eV to 2.55 ± 0.03 eV. The photoluminescence spectra shows broad and sharp emission peaks in violet, blue, green and greenish yellow range with PL intensities decreasing with increase in Co^{2+} concentration. The in-depth analysis of PL spectrum further substantiates replacement of Zn^{2+} by Co^{2+} in the ZnO matrix. PL lifetimes of these emissions were found to range between 6μ Sec to 9μ Sec which are considerably higher than reported data. However, on an average, the PL lifetime increases with increase in emission wavelengths. Thus the investigations affirm that the DMS nanoparticle material prepared by combustion method is monophasic, impurity free and displays superior ferromagnetic properties. The material has both semiconductor and ferromagnetic properties hence can be useful in variety of applications.

References

[1] D.P. Norton, Y.W. Heo, M.P. lvill, K. lp, S.J. Pearton, M.F. Chrisholm, T. Steiner, ZnO growth doping and processing, 7 (6) (2004) 34–40.
[2] A.S. Haja Hameed, C. Karthikeyan, S. Sasikumar, V. Senthil Kumar, S. Kumaresan, G. Ravi, Impact of alkaline metal ions Mg^{2+}, Ca^{2+}, Sr^{2+} and Ba^{2+} on the structural, optical, thermal and antibacterial properties of zno nanoparticles prepared by the Co-precipitation method, J. Mater. Chem. B (2013) 15950–15962.
[3] S.A. Wolf, D.D. Awschalom, R.A. Buhrman, J.M. Daughton, S. von Molna´r, M.L. Roukes, A.Y. Chtchelkanova, D.M. Treger, Spintronics: a spin-based electronics vision for the future, Science 294 (2001) 1488.
[4] Gertrude Neumark, Yinyan Gong, Igor Kuskovsky, Doping Aspects of Zn-based Wide-band-Gap Semiconductors Handbook of Electronic and Photonic Materials, Springer, 2007, pp. 843–854.
[5] J. Cao, J. Wu, Strain effects in low-dimensional transition metal oxides, Mater. Sci. Eng. 71 (2011) 35–52.
[6] Lin Wang Zhong, Zinc oxide nanostructures: growth, properties and applications, J. Phys. Condens. Matter 16 (25) (2004) 829–858.
[7] L. Schmidt-mende, Judith L. Macmanus-driscoll, ZnO – nanostructures defects and devices, mater, Today 10 (5) (2007) 40–48.
[8] J. Wellings, N. Chaure, S. Heavens, Dharmadasa, growth and characterisation of electrodeposited zno thin films, Thin Solid Films 516 (12) (2008) 3893–3898.
[9] Ü. Özgür, Ya I. Alivov, C. Liu, A. Teke, M.A. Reshchikov, S. Doğan, V. Avrutin, S.-J. Cho, H. Morkoç, A comprehensive review of ZnO materials and devices, J. Appl. Phys. 98 (4) (2005) 041301.
[10] A.M. Moezzi, M.B. Mcdonagh, Cortie, zinc oxide particles: synthesis, properties and applications, Chem. Eng. J. 185 (2012) 1–22.
[11] Millaty Mustaqima, Chunli Liu, Zno-based nanostructures for diluted magnetic semiconductor, Turk. J. Phys. 38 (2014) 429–441.
[12] E. Liu, P. Xiao, J.S. Chen, B.C. Lim, L. Li, Ni doped ZnO thin films for diluted magnetic semiconductor materials, Curr. Appl. Phys. 8 (2008) 408–411.
[13] S.A. Ahmed, Structural, optical, and magnetic properties of mn-doped zno samples, Results Phys. 7 (2017) 604–610.
[14] Jianwei Wang, Jiaqi Wan, Kezheng Chen, Facile synthesis of superparamagnetic Fe-doped ZnO nanoparticles in liquid polyols, Mater. Lett. 64 (2010) 2373–2375.
[15] T.J. Castro, P.A.M. Rodrigues, A.C. Oliveira, F. Nakagomi, J. Mantilla, J.A.H. Coaquira, A. Franco Júnior, H.V.S. Pessoni, P.C. Morais, S.W. da Silva, Optical and magnetic properties of Co-doped ZnO nanoparticles and the onset of ferromagnetic order, J. Appl. Phys. 121 (2017) 013904.
[16] Anshu Singhal, S.N. Achary, J. Manjanna, S. Chatterjee, P. Ayyub, A.K. Tyagi, Chemical synthesis and structural and magnetic properties of dispersible cobalt- and nickel-doped ZnO nanocrystals, J. Phys. Chem. C 114 (2010) 3422–3430.
[17] Lü Yinyun, Zhou Qi, Luning Chen, Wenwen Zhan, Zhaoxiong Xie, Kuang Qin, Lansun Zheng, Templated synthesis of diluted magnetic semiconductors using transition metal ion-doped metal–organic frameworks: the case of Co-doped ZnO, CrystEngComm 18 (2016) 4121–4126.
[18] Anindita Samanta, M.N. Goswami, P.K. Mahapatra, Structural, optical, dielectric, magnetic and magnetoelectric properties of Co-doped ZnO nanoparticles, J Mater Sci: Mater Electron 27 (2016) 12271–12278.
[19] S.H.U. Yuldashev, H.C. Jeon, Y.H. Kwon, S.J. Lee, T.W. Kang, KhT. Igamberdiev, A study of the origin of weak ferromagnetism in $Zn_{1-xc}o_xo$, Jom (2014) 66.

[20] P.P. Naik, R.B. Tangsali, B. Sonaye, S. Sugur, Enrichment of magnetic alignment stimulated by Γ-radiation in core-shell type nanoparticle Mn-Zn ferrite, Aip Conf. Proc. 1512 (2013) 354–355.
[21] Pranav P. Naik, R.B. Tangsali, B. Sonaye, S. Sugur, Sustained augmentation in electrical properties of $Mn_xZn_{1-X}Fe_2O_4$ nanoparticles provoked by high energy gamma radiation, J. Nano. Adv. Mat. 3 (2015) 1–7.
[22] M. Nirmala, Anukaliani, Characterization of undoped and Co doped ZnO nanoparticles synthesized by dc thermal plasma method, Physica B 406 (2011) 911–915.
[23] V. Pazhanivelu, A. Paul Blessington Selvadurai, Yongsheng Zhao, R. Thiyagarajan, R. Murugaraj, Room temperature ferromagnetism in Mn doped ZnO: Co nanoparticles by co-precipitation method, Physica B 481 (2016) 91–96.
[24] Rongliang He, Bin Tang, Cuong Ton-That, Matthew Phillips, Takuya Tsuzuki, Physical structure and optical properties of Co-doped ZnO nanoparticles prepared by Co-precipitation, J Nanopart Res 15 (2013).
[25] Umadevi Godavarti, V.D. Mote, Madhavaprasad Dasari, Role of cobalt doping on the electrical conductivity of ZnOnanoparticles, Journal of Asian Ceramic Societies (2017).
[26] Jun-Liang Zhao, Highly (002)-oriented zno film grown by ultrasonic spray pyrolysis on zno-seeded Si (100) substrate, J. Mater. Res 21 (2006) 2185–2190.
[27] Sanjeev Kumar, C.L. Chen, C.L. Dong, Y.K. Ho, J.F. Lee, T.S. Chan, R. Thangavel, T.K. Chen, B.H. Mok, S.M. Rao, M.K. Wu, Structural, optical, and magnetic characterization of Co and Co-doped ZnO nanopowders, J mater sci 48 (2013) 2618–2623.
[28] O.D. Jayakumar, I.K. Gopalakrishnan, S.K. Kulshreshtha, The structural and magnetization studies of Co-doped ZnO co-doped with Cu: synthesized by co precipitation method, J. Mater. Chem. 15 (2005) 3514–3518.
[29] S. Udayakumar, V. Renuka, K. Kavitha Structural, Optical and thermal studies of cobalt doped hexagonal ZnO by simple chemical precipitation method, J. Chem. Pharm. Res. 4 (2) (2012) 1271–1280.
[30] A.K. Srivastava, R. Gakhar, P. Dua, K. Senthil, J.S. Tawale, K.N. Sood, K. Yong, Structural Determination of Zn-O Dumbbells in Facetted Nano-particles, Microscopy: Science, Technology, Applications and Education, (1820).
[31] Khalid Hellal Harbbi, Ahmed alaa Ihsan, restriction of particle size and lattice strain through X-ray diffraction peak broadening analysis of ZnO nanoparticles, Advances In Physics Theories And App lications 49 (2015).
[32] Hiten Sarma, K.C. Sarma, X-ray peak broadening analysis of zno nanoparticles derived by precipitation method, International Journal Of Scientific And Research Publications 4 (2014).
[33] Sonal Singhal, Japinder Kaur, Tsering Namgyal, Rimi Sharma, Cu-doped ZnO nanoparticles: synthesis, structural and electrical properties, Physica B 407 (2012) 1223–1226.
[34] R.W. Kelsall, I.W. Hamley, M. Geoghegan, Nanoscale Science and Technology, John Wiley & Sons, 2006.
[35] Harish Kumar, Renu Rani, Structural characterization of silver nanoparticles synthesized by micro emulsion route, International Letters Of Chemistry, Physics And Astronomy 14 (2013) 26–36.
[36] P. Davide Cozzoli, M. Lucia Curri, andAngela Agostiano, ZnO nanocrystals by a non-hydrolytic route: synthesis and characterization, J. Phys. Chem. B 107 (2003) 4756 − 4762.
[37] G. Xiong, U. Pal, J.G. Serrano, K.B. Ucer, R.T. Williams, Photoluminescence and FTIR study of zno nanoparticles, the impurity and defect perspective, Phys Stat Sol C 3 (2006) 3577–3581.
[38] Atul B. Lavand, Yuvraj S. Malghe, Synthesis, characterization and visible light photocatalytic activity of carbon and iron modified ZnO, Journal Of King Saud University – Science (2016).
[39] Hao Yao-Ming, Shi-Yun Lou, Shao-Min Zhou, Rui-Jian Yuan, Gong-Yu Zhu, Li Ning, Structural, optical, and magnetic studies of manganese-doped zinc oxide hierarchical microspheres by self-assembly of nanoparticles, Nanoscale Research Letters 7 (2012) 100.
[40] K. Hyodo, S. Morimoto, T. Yamazaki, T. Ishikawa, J. Utsumi, Y. Ichiyanagi, Local structure analysis of diluted magnetic semiconductor Co and Al co-doped ZnO nano-particles, AIP Conference Proceedings 1709 (2016) 020004.
[41] Sasanka Deka, P.A. Joy, Synthesis and magnetic properties of Mn doped ZnO nanowires, Solid State Communications 142 (2007) 190–194.
[42] Jacek Wojnarowicz, Sylwia Kusnieruk, Tadeusz Chudoba, Stanislaw Gierlotka, Witold Lojkowski, Wojciech Knoff, Malgorzata Lukasiewicz, Bartlomiej Witkowski, Wolska Anna, T. Marcin, Klepka , Tomasz Story and Marek Godlewski, Paramagnetism of cobalt-doped zno nanoparticles obtained by microwave solvothermal synthesis, beilstein j. Nanotechnol. 6 (2015) 1957–1969.
[43] X.F. Wang, J.B. Xu, B. Zhang, H.G. Yu, J. Wang, X. Zhang, J.G. Yu, Q. Li, Signature of intrinsic high-temperature ferromagnetism in cobalt-doped zinc oxide nanocrystals, Adv. Mater. 18 (2006) 2476–2480.
[44] S. Fabbiyola, L. John Kennedy, Udaya Aruldoss, M. Bououdina, A.A. Dakhel, J. JudithVijaya, Synthesis of Co-doped ZnO nanoparticles via co-precipitation: structur-al,optical and magnetic properties, Powder Technology 286 (2015) 757–765.
[45] Sabiu Said Abdullahi, Yuksel Koseog˘lu, Sadik Guner, Sinan Kazan, Bayram Kocaman, E. Chifu, Ndikilar, Synthesis and characterization of Mn and Co codoped ZnO nanoparticles, Superlattices and Microstructures 83 (2015) 342–352.
[46] Yüksel Köseo˘glu, Enhanced Ferromagnetic Properties of Co-doped ZnO DMS Nanoparticles J Supercond Nov Magn, (2014).
[47] L.B. Duan, G.H. Rao, J. Yu, Y.C. Wang, Ferromagnetism of lightly Co-doped ZnO nanoparticles, Solid State Communications 145 (2008) 525–528.
[48] Anupama Chand, Shipra Gupta, M. Vasundhara, Shalik R. Joshi, Geeta R. Muttae, Jai Singh, Study of structural, optical and magnetic properties of cobalt doped ZnO nanorods, RSC Adv 7 (2017) 50527–50536.
[49] A. Franco Jr., H.V.S. Pessoni, P.R.T. Ribeiro, F.L.A. Machado, Magnetic properties of Co-doped ZnO nanoparticles, Journal of Magnetism and Magnetic Materials 426 (2017) 347–350.
[50] bin tang Rong liang he, cuong ton-that, Physical structure and optical properties of co-doped zno nanoparticles prepared by co-precipitation, j nanopart res 15 (2013) 1–8.
[51] S. Lakshmi Reddy, Tamio Endo, G. Siva Reddy, Electronic (Absorption) Spectra of 3d Transition Metal Complexes, Advance Aspects of Spectroscopy, INTECH, 2012.
[52] R. Elilarassi, G. Chandrasekaran, Influence of co-doping on the structural, optical and magnetic properties of ZnO nanoparticles synthesized using auto-combustion method, J Mater Sci: Mater Electron 24 (2013) 96–105.
[53] Anil Tumuluri, K. Lakshun Naidu, K.C. James Raju, Band gap determination using tauc's plot for $liNbo_3$, thin films international journal of chemtech research coden (USA) 6 (2014) 3353–3356.
[54] Anju Anna Jacob, L. Balakrishnan, K. Shambavi, Z.C. Alex, Multi-band visible photoresponse study of Co^{2+} doped ZnO nanoparticles, RSC Adv 7 (2017) 39657.
[55] T. Thangeeswari, Ann Tresa George and A. Arun Kumar, Optical properties and FTIR studies of cobalt doped ZnO nanoparticles by simple solution method, Indian journal of science and technology (2016) 9.
[56] M. Naeem, S.K. Hasanain, A. Mumtaz, Electrical transport and optical studies of ferromagnetic cobalt doped zno nanoparticles exhibiting a metal–insulator transition, J. Phys.: Condense Matter 20 (2008).
[57] Abdub G. Ali, Francis B. Dejene, Hendrik C. Swart, Effect of mn doping on the structural and optica properties of sol-gel derived zno nanoparticles, Cent. Eur. J. Phys 10 (2) (2012) 478–484.
[58] Amy L. Linsebigler, Guangquan Lu, John T. Yates Jr., Photocatalysis on Ti02 surfaces: principles, mechanisms, and selected results, Chem. Rev 95 (1995) 735–758.
[59] G. Vijayaprasath, R. Murugan, Y. Hayakawa, G. Ravi, Optical and magnetic studies on Gd doped ZnO nanoparticles synthesized by co-precipitation method, Journal of Luminescence 178 (2016) 375–383.
[60] S. Taguchi, T. Tayagaki, Y. Kanemitsu, Luminescence and magnetic properties of Co doped ZnO nanocrystals, Materials Science and Engineering 6 (2009) 012029.
[61] F.S. Husairi, Syahirah Mhd Ali, A. Azlinda, M. Rusop, S. Abdullah, Special effect of urea as a stabilizer in thermal immersion method to synthesis porous zinc oxide nanostructures, Hindawi Publish. Corp. J. Nanomater. 7 (2013).
[62] P.S. Xu, Y.M. Sun, C.S. Shi, F.Q. Xu, H.B. Pan, Native point defect states in ZnO, Sci. China,Ser 44 (2001) 1252–1253.
[63] T. Hammad, Jamil K. Salem, R.G. Harrison, Structure, optical properties and synthesis of Co-doped zno superstructures, Appl Nanosci 3 (2013) 133–139.
[64] R. Raji, K.G. Gopchandran, Zno nanostructures with tunable visible luminescence: effects of kinetics of chemical reduction and annealing, journal of science: advanced materials and devices 2 (2017) 51–58.
[65] X. Jiang, X. Zhao, L. Duan, H. Shen, H. Liu, T. Hou, F. Wang, Enhanced photoluminescence and photocatalytic activity of $ZnOZnWO_4$ nanocomposites synthesized by a precipitation method, Ceram. Int. 42 (2016) 15160–15165.

[66] Gang xiong, u. Pal, j. Garcia serrano, Correlations among size, defects, and photoluminescence in ZnO nanoparticles, journal of applied physics 101 (2007) 024317.
[67] Sunandan Baruah, Sudarson Sekhar Sinha, Barnali Ghosh, Samir Kumar Pal, A.K. Raychaudhuri, Joydeep Dutta, Photoreactivity of ZnO nanoparticles in visible light: effect of surface states on electron transfer reaction, Journal Of Applied Physics 105 (2009) 074308.
[68] Harish chander, santa chawla, Time resolved spectroscopic studies on some nanophosphors, bull. Mater. Sci. 31 (2008) 401–407.
[69] S.H. Keluskar, R.B. Tangsali, G.K. Nalk, J.S. Budkuley, High permeability of low loss Mn-Zn ferrite obtained by sintering nanoparticle Mn-Zn ferrite, Journal of Magnetism and Magnetic Materials 305 (2006) 296–303.
[70] J. Singh, A. Chanda, S. Gupta, P. Shukla, V. Chandra, Effect of cobalt doping on structural and optical properties of ZnO nanoparticles, AIP Conference Proceedings 1731 (2016) 050091.
[71] Azra Parveen, Shraddha Agrawal, Ameer Azam, Band gap tuning and fluorescence properties of lead sulfide $Pb_{0.9}A_{0.1}S$ (A: Fe, Co, and Ni) nanoparticles by transition metal doping, Optical Materials 76 (2018) 21–27.